The Journal of Chemical Physics COMMUNICATION pubs.aip.org/aip/jcp

Magnetochiroptical nanocavities in hyperbolic metamaterials enable sensing down to the few-molecule level

Cite as: J. Chem. Phys. 160, 071104 (2024); doi: 10.1063/5.0183806
Submitted: 24 October 2023 • Accepted: 28 January 2024 •
Published Online: 21 February 2024

William O. F. Carvalho,[1] Osvaldo N. Oliveira, Jr.,[1] and J. R. Mejía-Salazar[2,a)]

AFFILIATIONS

[1] Sao Carlos Institute of Physics, University of Sao Paulo, CP 369, 13560-970 São Carlos, SP, Brazil
[2] National Institute of Telecommunications (Inatel), Santa Rita do Sapucaí, MG 37540-000, Brazil

Note: This paper is part of the JCP Special Topic on Chirality of Plasmonic Structures and Materials.
[a)] **Author to whom correspondence should be addressed:** jrmejia@inatel.br

ABSTRACT

In this work, we combine the concepts of magnetic circular dichroism, nanocavities, and magneto-optical hyperbolic metamaterials (MO-HMMs) to demonstrate an approach for sensing down to a few molecules. Our proposal comprises a multilayer MO-HMM with a square, two-dimensional arrangement of nanocavities. The magnetization of the system is considered in polar configuration, i.e., in the plane of polarization and perpendicular to the plane of the multilayer structure. This allows for magneto-optical chirality to be induced through the polar magneto-optical Kerr effect, which is exhibited by reflected light from the nanostructure. Numerical analyses under the magnetization saturation condition indicate that magnetic circular dichroism peaks can be used instead of reflectance dips to monitor refractive index changes in the analyte region. Significantly, we obtained a relatively high sensitivity value of $S = 40$ nm/RIU for the case where refractive index changes are limited to the volume inside nanocavities, i.e., in the limit of a few molecules (or ultralow concentrations), while a very large sensitivity of $S = 532$ nm/RIU is calculated for the analyte region distributed along the entire superstrate layer.

I. INTRODUCTION

Chirality refers to the phenomenon where a pair of objects that are mirror images of each other cannot be superimposed under any type of geometric transformation. Chiral molecules such as amino acids, proteins, and DNA are ubiquitous in biological and biochemical processes.[1,2] Therefore, recognition and separation of enantiomers is crucial for applications in pharmaceuticals since the therapeutic effects of a chiral drug are often associated with a single enantiomer, whereas the other is inactive and/or toxic.[3] Molecular chirality is normally investigated using circular dichroism (CD),[4] but the signals are only measurable for large sample volumes or large molecules. This occurs due to the mismatch between the size of the molecules and the wavelength of the incident light, which produces weak light–matter interactions. Mechanisms that enable the detection and discrimination of chiral molecules down to the few-molecule level have been explored,[5] mostly based on enhanced, localized optical fields in chiral all-dielectric/plasmonic platforms.[6–9] The sensitivity of these chiral nanophotonic structures is hampered by the corresponding background CD signal. To overcome the latter drawback, researchers exploit the extrinsic chirality, i.e., optical chirality, from chiral near-field distributions in achiral nanostructures (under obliquely incident light).[10–12] Indeed, chiral near-fields with zero far-field CD have been demonstrated using achiral systems,[13] eliminating background signals for improved sensitivity. However, the passive nature of conventional achiral nanostructures still limits their applications.

Attempts to develop active achiral systems, i.e., achiral nanostructures with dynamically tunable CD, include the use of phase-change materials,[14] chemical reactions,[15] and magneto-optical (MO) effects (also called magnetochiroptical effects).[16,17] In comparison to temperature changes to manipulate phase-change materials and the use of chemical reagents, magnetochiroptical effects can not only be manipulated faster but also enable packaging via on-chip integrated electromagnetic coils.[18] Moreover, magnetic anisotropy combined with material anisotropies produces unusual MO effects,

as in MO hyperbolic metamaterials (MO-HMMs).[19–24] HMMs are artificial uniaxial materials with one of the principal components of the permittivity tensor (ε) with the opposite sign to the other two,[25] i.e., HMMs simultaneously exhibit dielectric and plasmonic properties. This unique feature enables the excitation of the so-called bulk plasmon polariton (BPP) modes, which are guided plasmonic resonances with their electromagnetic fields largely concentrated in the volume of the metamaterial slab. BPP resonances in non-magnetic HMMs have been used for biosensing with high sensitivity,[26–29] while unprecedented resolution levels were observed with the transverse MO Kerr effect (TMOKE) in MO-HMMs.[30] In fact, TMOKE has been used in the last few decades for the highly sensitive detection of biomolecules.[31–34] Those concepts were demonstrated for the analyte region throughout the entire superstrate medium; that is, these approaches are still limited to relatively large sample concentrations. On the other hand, recent works have demonstrated improved detection capabilities when using gratings[35] or nanocavities in HMMs.[5] In the latter approach, nanocavities functioned as plasmonic nanocuvettes in which the analyte molecules were placed, thus reducing the analyte region to the volume of the nanocavities. One limitation of the latter approach, though, is the need to label fluorophores in the nanocuvettes.

In this work, we overcome these drawbacks by combining the concepts of plasmonic nanocavities and achiral MO-HMMs in what we call magnetochiroptical nanocavities. We demonstrate numerically the possibility of detecting a few tens of high-refractive-index achiral nanospheres inside the cavity volumes, which opens up the possibility for label-free (bio)sensing down to the few-molecule level. Our approach uses magnetic CD (MCD) peaks,[36] instead of plasmonic resonances, to monitor refractive index changes. Although most calculations in this work were made for achiral analytes, we numerically demonstrate that higher sensitivities are expected when using chiral molecules, where MCD will not only be affected by the applied magnetic fields but also by the chirality of the analyte. It is noteworthy that leveraging magnetochiroptical effects selectively amplifies the MCD amplitude for distinct enantiomers, thereby enhancing the measured MCD signal associated with each.

II. METHODOLOGY

A schematic representation of the nanostructure is shown in Fig. 1(a). A helix-like arrow is used to illustrate an incident right circularly polarized (RCP) optical field. Magnetization ($\mathbf{M}$) is represented by an arrow that can point up or down, perpendicular to the plane of the structure. The metasurface comprises a square network of elliptical nanocavities carved into a multilayer of alternating slabs of silver (Ag) and cerium-substituted yttrium iron garnet (Ce:YIG), grown on a substrate of silica (SiO_2). The geometrical parameters are shown in the upper and side views in Figs. 1(b)–1(c), where the two-dimensional periods with lengths Λ_x and Λ_y along the x- and y-axes, respectively, are illustrated. The major and minor axes of the elliptical nanocavities are labeled p_x and p_y. Note that the perforation depths were taken up to the substrate surface in all calculations. The cross section view in Fig. 1(c) depicts a multilayer consisting of three ($N = 3$) alternated Ag–Ce:YIG bilayers, having single layer thicknesses t_{Ag} and $t_{Ce:YIG}$. As demonstrated in Ref. 30, a multilayer with $N = 3$ is sufficient to produce an effective hyperbolic dispersion,

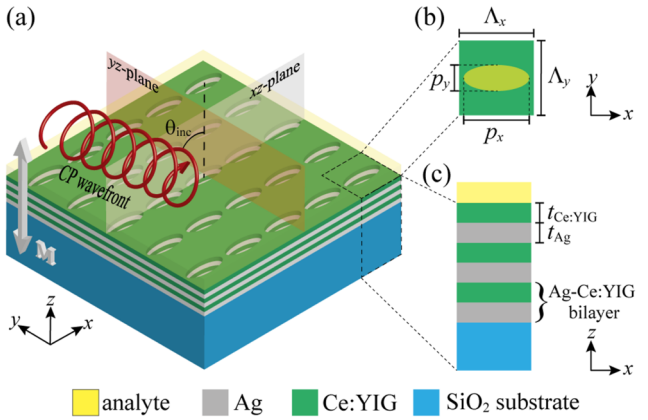

FIG. 1. Schematic representation of the nanostructure. (a) CP incident wavefront impinges the MO-HMM metasurface on a square lattice array of elliptical holes carved in heterogeneous alternated Ag–Ce:YIG bilayers. (b) Upper and (c) side views with geometric parameters.

i.e., $\varepsilon_{\parallel}\varepsilon_{\perp} < 0$ (subindexes $\parallel$ and $\perp$ should be understood with reference to the xy-plane). Therefore, we first optimized the parameters t_{Ag} and $t_{Ce:YIG}$ to exhibit HMM behavior in a broad wavelength range covering $\lambda = 900$ nm,[30] where the dielectric material Ce:YIG exhibits its maximum MO activity. Such optimization was carried out using electromagnetic simulations through the finite element method (FEM) using the commercial software COMSOL Multiphysics. We used an automated optimization algorithm within the software COMSOL to find the geometric parameters of the nanocavities that lead to maximum MO activity around the wavelength 900 nm. The parameters are $\Lambda = 375$ nm for the period, $p_x = 330$ nm and $p_y = 130$ nm for the major and minor axes of the elliptical nanocavities, and $t_{Ag} = t_{Ce:YIG} = 100$ nm for the Ag and Ce:YIG layer thicknesses. Since the multilayer in Fig. 1(a) is achiral, we use the magnetic circular dichroism (MCD) parameter (in degrees),[6]

$$\mathrm{MCD}\ (^\circ) = \tan^{-1}\left(\frac{R_{RCP} - R_{LCP}}{R_{RCP} + R_{LCP}}\right), \tag{1}$$

to quantify the magnetically induced chirality of the system. We measured MCD in reflectance, and R_{RCP} and R_{LCP} represent reflectances for RCP and LCP (left circularly polarized) incident wavefronts, respectively. Under these conditions, the superstrate (i.e., the dielectric material above the structure) will be the analyte region. The latter is possible because the elliptical nanocavities will work not only as nanocuvettes for probing small analyte concentrations but as gratings for light-nanostructure coupling. The resonant coupling can be represented through a phase-matching condition, which for the square photonic lattice ($\Lambda_x = \Lambda_y = \Lambda$) in this work can be written as[37]

$$k^2 = \left[\frac{2\pi}{\lambda} n_a \sin(\theta_{inc}) \cos(\phi_{inc}) + p\frac{2\pi}{\Lambda}\right]^2 + \left[\frac{2\pi}{\lambda} n_a \sin(\theta_{inc}) \cos(\phi_{inc}) + n\frac{2\pi}{\Lambda}\right]^2 = k_x^2 + k_y^2 \tag{2}$$

with

$$k_x = \frac{2\pi}{\lambda} n_a \sin(\theta_{inc}) \cos(\phi_{inc}) + p\frac{2\pi}{\Lambda}, \quad (3)$$

$$k_y = \frac{2\pi}{\lambda} n_a \sin(\theta_{inc}) \cos(\phi_{inc}) + n\frac{2\pi}{\Lambda}, \quad (4)$$

where $k_x = k_y = (2\pi/\lambda)n_a \sin(\theta_{p,n})\cos(\phi_{p,n})$ are the reflected wavevectors. θ_{inc} and ϕ_{inc} are the incident angles in the xz- and yz-planes, respectively. p and n are the integer numbers denoting the diffraction orders, λ is the working wavelength, Λ is the period length, and n_a is the refractive index of the analyte region (the dielectric region above the system). Results are calculated using circularly polarized incident fields with electric field amplitudes $\mathbf{E} = (E_x\hat{\mathbf{x}} \pm iE_y\hat{\mathbf{y}})e^{-i\mathbf{k}_{inc}\cdot\mathbf{r}}$, where the sign +/− denotes the RCP/LCP state. The permittivity values for the SiO_2 (ε_{SiO_2})[38] and Ag (ε_{Ag})[39] were used from experimental results.

Since $\mathbf{M}$ is considered to be pointing along the $\pm z$-axis, the permittivity tensor for the Ce:YIG layers is defined as[40]

$$\tilde{\varepsilon}_{Ce:YIG} = \begin{pmatrix} \varepsilon_{Ce:YIG} & im\varepsilon_{xy} & 0 \\ -im\varepsilon_{yx} & \varepsilon_{Ce:YIG} & 0 \\ 0 & 0 & \varepsilon_{Ce:YIG} \end{pmatrix}, \quad (5)$$

which is also dependent on the incident wavelength. For example, for $\lambda = 900$ nm, $\varepsilon_{Ce:YIG} = 5.26 + i0.32$ for the diagonal and $\varepsilon_{xy} = \varepsilon_{yx} = -0.003 + i0.042$ off-diagonal components.[40] $m = \pm 1$ is used to indicate that the magnetization is pointing along the $\pm z$-axis. All calculations were made under the magnetization saturation condition, which in Ce:YIG is reached using magnetic fields around $B = 2$ kOe.[40] Floquet periodic boundary conditions were set to consider an infinitely periodic system along the xy-plane. Perfectly matched layers (PMLs) are used along the z-boundaries to avoid spurious numerical reflections. Results were obtained within the incident wavelength range of $600 \le \lambda \le 1250$ nm for normal and oblique incidence over the MO-HMM. Three incident wave configurations were used: ($\theta_{inc} = 0°$; $\phi_{inc} = 0°$), ($\theta_{inc} = 45°$; $\phi_{inc} = 0°$), or ($\theta_{inc} = 0°$; $\phi_{inc} = 45°$).

III. RESULTS AND DISCUSSION

The reflectances for the three incidence conditions, i.e., for ($\theta_{inc} = 0°$; $\phi_{inc} = 0°$), ($\theta_{inc} = 45°$; $\phi_{inc} = 0°$), and ($\theta_{inc} = 0°$; $\phi_{inc} = 45°$), are given in Fig. 2. Numerical data are shown for $m = 0$ (in other words, the system is demagnetized) and $m = +1$ (the system is magnetized along the $+z$-axis). For RCP reflectance (under oblique incidence), dips appear near $\lambda = 900$ nm, which are related to the excitation of BPP resonances in the multilayer HMM structure. Magnetochiroptical effects are observed in Figs. 2(b)–2(d), where reflectances for RCP and LCP waves are shown for the three incidence conditions with $m = +1$. At normal incidence, i.e., $\theta_{inc} = \phi_{inc} = 0°$, an MCD peak is observed just around $\lambda = 900$ nm (see Fig. 3), as expected from geometric optimization. The last peak is due to the largest difference between the reflectance curves for RCP and LCP waves for wavelengths between the modes BPP_1 and BPP_2 in Fig. 2(c). Resonant shifts are observed in Fig. 3 for obliquely incident fields, induced through small changes in

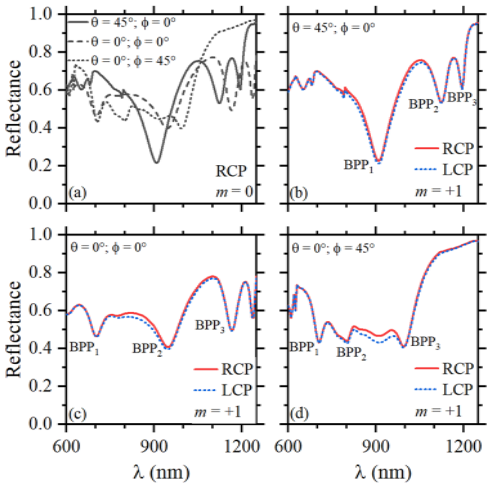

FIG. 2. (a) RCP reflectances according to three incident angles and $m = 0$. RCP and LCP reflectances for $m = +1$ for (b) $\theta_{inc} = 45°$; $\phi_{inc} = 0°$, (c) $\theta_{inc} = 0°$; $\phi_{inc} = 0°$, and (d) $\theta_{inc} = 0°$; $\phi_{inc} = 45°$.

the phase-matching condition [see Eq. (2)]. Moreover, due to the combined contribution from BPP resonances and magnetochiroptical effects, higher MCD amplitudes are obtained under oblique incidence. In particular, MCD amplitudes for $\theta_{inc} = 0°$; $\phi_{inc} = 45°$ and $\theta_{inc} = 45°$; $\phi_{inc} = 0°$ achieve values (for both $m = \pm 1$) up to $\pm 2.31°$ and $\pm 2.23°$, respectively, which are competitive with recent reports using chiral nanostructures comprising magnetoplasmonic helicoids on a dielectric substrate.[41]

Motivated by the possibility of exploiting MCD peaks for (bio)sensing applications, we focus our attention on the incidence conditions ($\theta_{inc} = 45°$; $\phi_{inc} = 0°$) due to the sharper MCD peak (see Fig. 3). Furthermore, BPP resonances have their electromagnetic fields distributed inside the volume of the HMM and, consequently, inside the nanocavity volume. In fact, the latter is demonstrated in Fig. 4, where calculations of the normalized resonant electromagnetic near-field distributions are presented. The top panel (bottom panel), labeled Fig. 4(a) [Fig. 4(b)], shows the modulus of the resonant magnetic near-field distribution $|H|$ for a RCP (LCP) incident wave. Differences associated with the near-field chirality of both polarizations are noted in the comparison in Fig. 4.

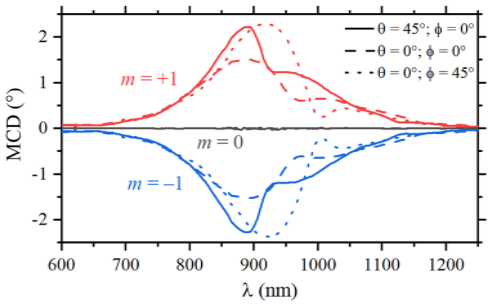

FIG. 3. MCD for three incident angles, considering $m = +1$ in red, $m = -1$ in blue, and $m = 0$ in black (no circular dichroism).

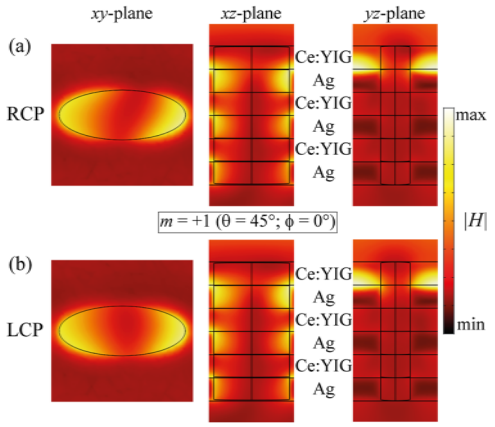

FIG. 4. Normalized *H*-field on MO-HMM metasurface with $N = 3$ at BPP resonance. *xy*-, *xz*- and *yz*-plane views for (a) RCP and (b) LCP.

Since the characteristics of the MCD (amplitudes and positions in the spectrum) can be adapted and tuned with N, as shown in Fig. 5, we select $N = 3$ to obtain a balance between a high MCD and a cost-effective and easy-to-fabricate nanostructure.

Since the near-fields in Fig. 4 produce gradient optical forces that trap nearby nanoparticles inside the nanocavity volume,[42] one expects that in the case of low concentrations, the analyte molecules will become trapped in the nanocavities. Therefore, we start our analysis by assuming that refractive index changes only occur within the volume of the nanocavity, as shown in the inset in Fig. 6(b). The MCD curves and the corresponding spectral shifts as a function of n_a (varying from 1.33 up to 1.43 inside the nanocativy) are shown in Figs. 6(a) and 6(b), respectively. A sensitivity ($S(\lambda) = |\Delta\lambda_{res}/\Delta n_a|$) of 40 nm/RIU is inferred, which is a relatively high value for the conditions of the calculations. In contrast, if changes in refractive index are not limited to the nanocavity but throughout the entire superstrate region, the sensitivity is 532 nm/RIU, as demonstrated in Figs. 6(c)–6(d). Unlike other approaches exploiting polar MO configurations for ultrasensitive applications,[43] our concept does not require a combination of different techniques to monitor phase-changes.

We have also verified that our proposal is suitable to monitor refractive index changes induced by 21 nanospheres of radius 30 nm

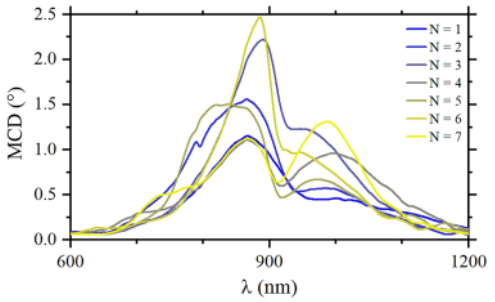

FIG. 5. MCD spectrum as a function of the number (N) of Ag–Ce:YIG bilayers.

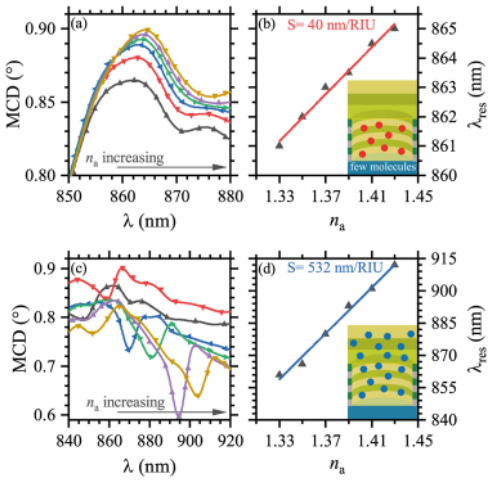

FIG. 6. MCD spectra and MCD peak shift as a function of the analyte refractive index, varying from $n_a = 1.33$ to $n_a = 1.43$, for the limits of (a)–(b) ultra-low concentration (few molecules) and (c)–(d) high concentration.

and refractive index $n_s = 2.0$. Hence, it is possible to detect concentrations as low as a few tens of molecules. Since these nanospheres are chiral, we calculated the corresponding MCD amplitude changes and resonance shifts associated with different values of chirality (κ), as shown in Fig. 7. Results are shown for $\kappa = 0, \pm 0.5, \pm 1$ in comparison with the extrinsic chirality of the structure (without molecules). Numerical simulations for chiral nanospheres were made using the constitutive equations in the Boys–Post form[44]

$$\mathbf{D} = \varepsilon\mathbf{E} + i\frac{\kappa}{c}\mathbf{B}, \tag{6}$$

$$\mathbf{H} = \frac{1}{\mu}\mathbf{B} + i\frac{\kappa}{c}\mathbf{E}, \tag{7}$$

where c is the speed of light in a vacuum.

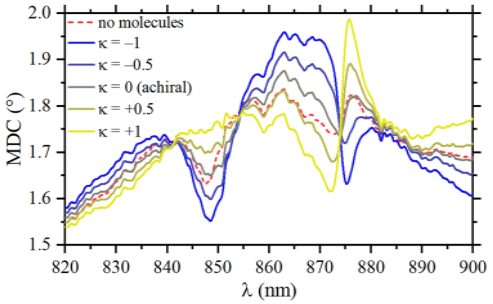

FIG. 7. MCD spectra calculated for 21 dielectric nanospheres of radius $r = 30$ nm and refractive index $n_s = 2.0$, distributed along the nanocavity. Numerical results are comparatively shown for $\kappa = 0, \pm 0.5, \pm 1$, and the system without molecules (dashed line).

IV. CONCLUSIONS

We have shown with numerical simulations that MCD peaks from an arrangement of nanocavities in a MO-HMM can be used for sensing. A proof of concept is demonstrated for two cases: (i) the analyte region is limited to the volume inside nanocavities, for which relatively high sensitivity values (S = 40 nm/RIU) were calculated, and (ii) the analyte region is distributed along the entire superstrate region, including the volume of the nanocavities, for which a very high sensitivity (S = 532 nm/RIU) is obtained. Since the proposed MO-HMM structure is surrounded by aqueous media, considering the analyte molecules limited to the volume of the nanocavities implicitly means that we are working with ultra-low concentration levels, i.e., we are only using a few analyte molecules in the sample. In contrast to other proposals using complementary fluorophore labeling for indirect detection through fluorescence spectroscopy, we only monitor the shifts of the MCD peaks due to small changes in the surrounding refractive index. It is worth noting that the nanocavity arrangement in the concept shown here also works as a grating coupler to allow the excitation of bulk plasmon polariton modes in the MO-HMM without the need for prism couplers, enabling straightforward integrability with microfluidic technology.

ACKNOWLEDGMENTS

This work was partially supported by RNP, with resources from MCTIC, Grant No. 01245.020548/2021-07, under the Brazil 6G project of the Radiocommunication Reference Center (Centro de Referência em Radiocomunicações—CRR) of the National Institute of Telecommunications (Instituto Nacional de Telecomunicações—Inatel), Brazil, and by Huawei, under the project Advanced Academic Education in Telecommunications Networks and Systems, Contract No. PPA6001BRA23032110257684. We also acknowledge the financial support from the Brazilian agencies National Council for Scientific and Technological Development-CNPq (Grant No. 314671/2021-8) and FAPESP (Grant Nos. 2018/22214-6, 2023/08999-9).

AUTHOR DECLARATIONS

Conflict of Interest

The authors have no conflicts to disclose.

Author Contributions

William O. F. Carvalho: Conceptualization (lead); Formal analysis (lead); Investigation (lead); Methodology (lead); Writing – original draft (equal). **Osvaldo N. Oliveira, Jr.**: Project administration (equal); Writing – review & editing (equal). **J. R. Mejía-Salazar**: Supervision (lead); Writing – original draft (equal); Writing – review & editing (equal).

DATA AVAILABILITY

The data that support the findings of this study are available from the corresponding author upon reasonable request.

REFERENCES

[1]J. McConathy and M. J. Owens, "Stereochemistry in drug action," The Primary Care Companion CNS Disord. **5**, 70 (2003).
[2]X. Du, J. Zhou, J. Wang, R. Zhou, and B. Xu, "Chirality controls reaction-diffusion of nanoparticles for inhibiting cancer cells," ChemNanoMat **3**, 17–21 (2017).
[3]A. Renslo and A. Renslo, *Stereochemistry* (McGraw-Hill Education, New York, 2016).
[4]E. Tokunaga, T. Yamamoto, E. Ito, and N. Shibata, "Understanding the thalidomide chirality in biological processes by the self-disproportionation of enantiomers," Sci. Rep. **8**, 17131 (2018).
[5]S. C. Indukuri, C. Frydendahl, N. Sharma, N. Mazurski, Y. Paltiel, and U. Levy, "Enhanced chiral sensing at the few-molecule level using negative index metamaterial plasmonic nanocuvettes," ACS Nano **16**, 17289–17297 (2022).
[6]E. Mohammadi, K. L. Tsakmakidis, A.-N. Askarpour, P. Dehkhoda, A. Tavakoli, and H. Altug, "Nanophotonic platforms for enhanced chiral sensing," ACS Photonics **5**, 2669–2675 (2018).
[7]W. A Paiva-Marques, F. Reyes Gómez, O. N Oliveira, Jr., and J. R. Mejía-Salazar, "Chiral plasmonics and their potential for point-of-care biosensing applications," Sensors **20**, 944 (2020).
[8]G. Palermo, G. E. Lio, M. Esposito, L. Ricciardi, M. Manoccio, V. Tasco, A. Passaseo, A. De Luca, and G. Strangi, "Biomolecular sensing at the interface between chiral metasurfaces and hyperbolic metamaterials," ACS Appl. Mater. Interfaces **12**, 30181–30188 (2020).
[9]F. Reyes Gómez, O. N. Oliveira, Jr., P. Albella, and J. R. Mejía-Salazar, "Enhanced chiroptical activity with slotted high refractive index dielectric nanodisks," Phys. Rev. B **101**, 155403 (2020).
[10]E. Plum, V. A. Fedotov, and N. I. Zheludev, "Optical activity in extrinsically chiral metamaterial," Appl. Phys. Lett. **93**, 191911 (2008).
[11]E. Plum, X.-X. Liu, V. A. Fedotov, Y. Chen, D. P. Tsai, and N. I. Zheludev, "Metamaterials: Optical activity without chirality," Phys. Rev. Lett. **102**, 113902 (2009).
[12]B. M. Maoz, A. Ben Moshe, D. Vestler, O. Bar-Elli, and G. Markovich, "Chiroptical effects in planar achiral plasmonic oriented nanohole arrays," Nano Lett. **12**, 2357–2361 (2012).
[13]A. Vázquez-Guardado and D. Chanda, "Superchiral light generation on degenerate achiral surfaces," Phys. Rev. Lett. **120**, 137601 (2018).
[14]S. Wang, L. Kang, and D. H. Werner, "Active terahertz chiral metamaterials based on phase transition of vanadium dioxide (VO2)," Sci. Rep. **8**, 189 (2018).
[15]M. Matuschek, D. P. Singh, H.-H. Jeong, M. Nesterov, T. Weiss, P. Fischer, F. Neubrech, and N. Liu, "Chiral plasmonic hydrogen sensors," Small **14**, 1702990 (2018).
[16]I. Zubritskaya, N. Maccaferri, X. Inchausti Ezeiza, P. Vavassori, and A. Dmitriev, "Magnetic control of the chiroptical plasmonic surfaces," Nano Lett. **18**, 302–307 (2018).
[17]J. Qin, L. Deng, T. Kang, L. Nie, H. Feng, H. Wang, R. Yang, X. Liang, T. Tang, J. Shen, C. Li, H. Wang, Y. Luo, G. Armelles, and L. Bi, "Switching the optical chirality in magnetoplasmonic metasurfaces using applied magnetic fields," ACS Nano **14**, 2808–2816 (2020).
[18]T. Murai, Y. Shoji, N. Nishiyama, and T. Mizumoto, "Nonvolatile magneto-optical switches integrated with a magnet stripe array," Opt. Express **28**, 31675–31685 (2020).
[19]I. A. Kolmychek, A. R. Pomozov, A. P. Leontiev, K. S. Napolskii, and T. V. Murzina, "Magneto-optical effects in hyperbolic metamaterials," Opt. Lett. **43**, 3917–3920 (2018).
[20]B. Fan, M. E. Nasir, L. H. Nicholls, A. V. Zayats, and V. A. Podolskiy, "Magneto-optical metamaterials: Nonreciprocal transmission and faraday effect enhancement," Adv. Opt. Mater. **7**, 1801420 (2019).
[21]X. Wang, H. Wang, J. Jian, B. X. Rutherford, X. Gao, X. Xu, X. Zhang, and H. Wang, "Metal-free oxide-nitride heterostructure as a tunable hyperbolic metamaterial platform," Nano Lett. **20**, 6614–6622 (2020).
[22]I. V. Malysheva, I. A. Kolmychek, A. M. Romashkina, A. P. Leontiev, K. S. Napolskii, and T. V. Murzina, "Magneto-optical effects in hyperbolic metamaterials based on ordered arrays of bisegmented gold/nickel nanorods," Nanotechnology **32**, 305710 (2021).

[23]X. Wang, J. Jian, H. Wang, J. Liu, Y. Pachaury, P. Lu, B. X. Rutherford, X. Gao, X. Xu, A. El-Azab, X. Zhang, and H. Wang, "Nitride-oxide-metal heterostructure with self-assembled core–shell nanopillar arrays: Effect of ordering on magneto-optical properties," Small **17**, 2007222 (2021).
[24]J. Kuttruff, A. Gabbani, G. Petrucci, Y. Zhao, M. Iarossi, E. Pedrueza-Villalmanzo, A. Dmitriev, A. Parracino, G. Strangi, F. De Angelis, D. Brida, F. Pineider, and N. Maccaferri, "Magneto-optical activity in nonmagnetic hyperbolic nanoparticles," Phys. Rev. Lett. **127**, 217402 (2021).
[25]M. Lobet, N. Kinsey, I. Liberal, H. Caglayan, P. A. Huidobro, E. Galiffi, J. R. Mejía-Salazar, G. Palermo, Z. Jacob, and N. Maccaferri, "New horizons in near-zero refractive index photonics and hyperbolic metamaterials," ACS Photonics **2023**, 10, 3805–3820.
[26]A. V. Kabashin, P. Evans, S. Pastkovsky, W. Hendren, G. A. Wurtz, R. Atkinson, R. Pollard, V. A. Podolskiy, and A. V. Zayats, "Plasmonic nanorod metamaterials for biosensing," Nat. Mater. **8**, 867–871 (2009).
[27]K. V. Sreekanth, Y. Alapan, M. ElKabbash, E. Ilker, M. Hinczewski, U. A. Gurkan, A. De Luca, and G. Strangi, "Extreme sensitivity biosensing platform based on hyperbolic metamaterials," Nat. Mater. **15**, 621–627 (2016).
[28]G. Palermo, K. V. Sreekanth, N. Maccaferri, G. E. Lio, G. Nicoletta, F. De Angelis, M. Hinczewski, and G. Strangi, "Hyperbolic dispersion metasurfaces for molecular biosensing," Nanophotonics **10**, 295–314 (2020).
[29]R. Yan, T. Wang, X. Yue, H. Wang, Y.-H. Zhang, P. Xu, L. Wang, Y. Wang, and J. Zhang, "Highly sensitive plasmonic nanorod hyperbolic metamaterial biosensor," Photonics Res. **10**, 84–95 (2022).
[30]B. F. Díaz-Valencia, N. Porras-Montenegro, O. N. J. Oliveira, Jr., and J. R. Mejía-Salazar, "Nanostructured hyperbolic metamaterials for magnetoplasmonic sensors," ACS Appl. Nano Mater. **5**, 1740–1744 (2022).
[31]D. O. Ignatyeva, G. A. Knyazev, P. O. Kapralov, G. Dietler, S. K. Sekatskii, and V. I. Belotelov, "Magneto-optical plasmonic heterostructure with ultranarrow resonance for sensing applications," Sci. Rep. **6**, 28077 (2016).
[32]M. G. Manera, A. Colombelli, A. Taurino, A. G. Martin, and R. Rella, "Magneto-optical properties of noble-metal nanostructures: Functional nanomaterials for bio sensing," Sci. Rep. **8**, 12640 (2018).
[33]C. Rizal, M. G. Manera, D. O. Ignatyeva, J. R. Mejía-Salazar, R. Rella, V. I. Belotelov, F. Pineider, and N. Maccaferri, "Magnetophotonics for sensing and magnetometry toward industrial applications," J. Appl. Phys. **130**, 230901 (2021).
[34]N. Maccaferri, A. Gabbani, F. Pineider, T. Kaihara, T. Tapani, and P. Vavassori, "Magnetoplasmonics in confined geometries: Current challenges and future opportunities," Appl. Phys. Lett. **122**, 120502 (2023).
[35]N. Maccaferri, T. Isoniemi, M. Hinczewski, M. Iarossi, G. Strangi, and F. De Angelis, "Designer Bloch plasmon polariton dispersion in grating-coupled hyperbolic metamaterials," APL Photonics **5**, 076109 (2020).
[36]F. Pineider, G. Campo, V. Bonanni, C. de Julián Fernández, G. Mattei, A. Caneschi, D. Gatteschi, and C. Sangregorio, "Circular magnetoplasmonic modes in gold nanoparticles," Nano Lett. **13**, 4785–4789 (2013).
[37]B. Zhou, W. Jia, C. Xiang, Y. Xie, J. Wang, G. Jin, Y. Wang, and C. Zhou, "Polarization-independent 2 × 2 high diffraction efficiency beam splitter based on two-dimensional grating," Opt. Express **29**, 32042–32050 (2021).
[38]I. H. Malitson, "Interspecimen comparison of the refractive index of fused silica," J. Opt. Soc. Am. **55**, 1205–1209 (1965).
[39]K. M. McPeak, S. V. Jayanti, S. J. P. Kress, S. Meyer, S. Iotti, A. Rossinelli, and D. J. Norris, "Plasmonic films can easily be better: Rules and recipes," ACS Photonics **2**, 326–333 (2015).
[40]M. C. Onbasli, L. Beran, M. Zahradník, M. Kučera, R. Antoš, J. Mistrík, G. F. Dionne, M. Veis, and C. A. Ross, "Optical and magneto-optical behavior of Cerium Yttrium Iron Garnet thin films at wavelengths of 200–1770 nm," Sci. Rep. **6**, 23640 (2016).
[41]J. W. Kim, N. H. Cho, R. M. Kim, J. H. Han, S. Choi, S. D. Namgung, H. Kim, and K. T. Nam, "Magnetic control of the plasmonic chirality in gold helicoids," Nano Lett. **22**, 8181–8188 (2022).
[42]A. N. Koya, J. Cunha, T.-L. Guo, A. Toma, D. Garoli, T. Wang, S. Juodkazis, D. Cojoc, and R. Proietti Zaccaria, "Novel plasmonic nanocavities for optical trapping-assisted biosensing applications," Adv. Opt. Mater. **8**, 1901481 (2020).
[43]N. Maccaferri, K. E Gregorczyk, T. V. De Oliveira, M. Kataja, S. Van Dijken, Z. Pirzadeh, A. Dmitriev, J. Åkerman, M. Knez, and P. Vavassori, "Ultrasensitive and label-free molecular-level detection enabled by light phase control in magnetoplasmonic nanoantennas," Nat. Commun. **6**, 6150 (2015).
[44]V. V. Klimov, I. V. Zabkov, A. A. Pavlov, and D. V. Guzatov, "Eigen oscillations of a chiral sphere and their influence on radiation of chiral molecules," Opt. Express **22**, 18564–18578 (2014).